



Influence of polar bridging molecules on the photoelectrocatalytic hydrogen production from perylene diimide network structures

Weixing Nie^a, Mengnan Ruan^{a,b,*}, Bo Li^c, Yuxin Sun^a, Ke Ruan^a, Xiaowei Liu^a, Zhifeng Liu^{a,b,*}

^a School of Materials Science and Engineering, Tianjin Chengjian University, Tianjin 300384, China

^b Tianjin Key Laboratory of Building Green Functional Materials, Tianjin 300384, China

^c Beijing Spacecraft, Beijing, China

ARTICLE INFO

Keywords:

Perylene diimide
Bridging molecules
 π - π stacking
DFT calculations

ABSTRACT

Perylene diimide (PDI) photocatalysts are characterized by with broad spectral response, assemblability of molecules, and tunable energy band structure, but the slowness of their photogenerated carriers within the catalysts limits further applications. In this paper, PDI-based photoelectrodes with triazine-pyrimidine-PDI (TPP) and triazine-benzene-PDI (TBP) structures formed by triazine-, pyrimidine- and benzene-conjugated PDIs were designed and prepared in order to improve the overall carrier transport efficiency and reactivity of the catalysts. The interaction of the bridging molecules triazine, pyrimidine and benzene in the system generates a spatial electric field, as demonstrated by density-functional theory (DFT) calculations and detailed experiments. In addition, TPP exhibited the best photoelectrocatalytic performance, in which the current density of TPP reached 0.637 mA/cm² at 1.23 V vs. RHE, which was 10.79 times higher than that of pure triazine-PDI (TP). This study will provide new ideas for the application of photocatalysts of PDI polymers in new energy fields.

1. Introduction

Photoelectrocatalytic technology is a promising technology for cracking water to produce hydrogen with the advantages of clean energy availability, reusability and low energy consumption [1–3]. Inorganic metal oxide compounds, especially titanium dioxide (TiO₂), have been widely studied and applied in the past decades [4]. However, the future development of such catalysts is somewhat limited by the fact that metal resources are usually difficult to regenerate and the ability to modify the functional groups and properties of the catalysts is restricted. Therefore, organic photocatalysts (polythiophene, porphyrin and perylenediimide, etc.) are gradually becoming the first choice for new energy catalysis due to their diverse chemical modification sites and abundant elemental reserves [5–7].

Perylenediimide (PDI)-based photocatalysts have gradually become the focus of research due to their broad spectral response, tunable molecular structure and assembly [8–10]. PDI molecules consist of carboxylated imides on both sides and rigid polyaromatic ring nuclei, and the electron-withdrawing imide groups are combined with conjugated structural polyaromatic ring nuclei, which are conducive to the migration of carriers [11,12]. During the catalytic process, it takes hundreds of picoseconds for photogenerated carriers to be transported

from the interior to the surface, whereas light-generated electron-hole complexation in the bulk phase takes only a few picoseconds. The charge separation and transport efficiency of PDI directly affects its photoelectrocatalytic performance [13,14]. Therefore, it is essential to design rational PDI-based photocatalysts to achieve effective charge separation.

The use of covalent bonds to connect PDI molecules in a certain direction is an efficient PDI modification strategy [15,16]. It not only improves the intermolecular connection stability, but also preserves the intramolecular electron transfer channels (π -domain channels). Zhang et al. [17] by linking PDI single molecules with covalent bonds to form PDI polymers, succeeded in preparing an efficient urea-PDI polymer photocatalyst. A broad photoresponse, high photocatalytic hydrogen production rate and stability were demonstrated. Meanwhile, Zhang et al., [18] prepared ethylene-PDI, hydrazine-PDI and triazine-PDI polymers by linking the amide position of PDI with ethylenediamine, hydrazine hydrate and melamine, respectively. The dipole moment and spatial electric field strength of triazine-PDI were found to be larger than those of ethylene-PDI and hydrazine-PDI, and the phenol degradation rate of triazine-PDI was much larger than that of the other two substances. Based on the above reports, some advantages of PDI polymers were proposed: (i) PDI-based polymers retained the intramolecular π -detachment channels to enhance the carrier mobility; (ii) the larger

* Corresponding authors at: School of Materials Science and Engineering, Tianjin Chengjian University, Tianjin 300384, China.

E-mail addresses: 15101175504@163.com (M. Ruan), tjulzf@163.com (Z. Liu).

<https://doi.org/10.1016/j.apcatb.2024.124242>

Received 6 May 2024; Received in revised form 22 May 2024; Accepted 24 May 2024

Available online 27 May 2024

0926-3373/© 2024 Elsevier B.V. All rights are reserved, including those for text and data mining, AI training, and similar technologies.

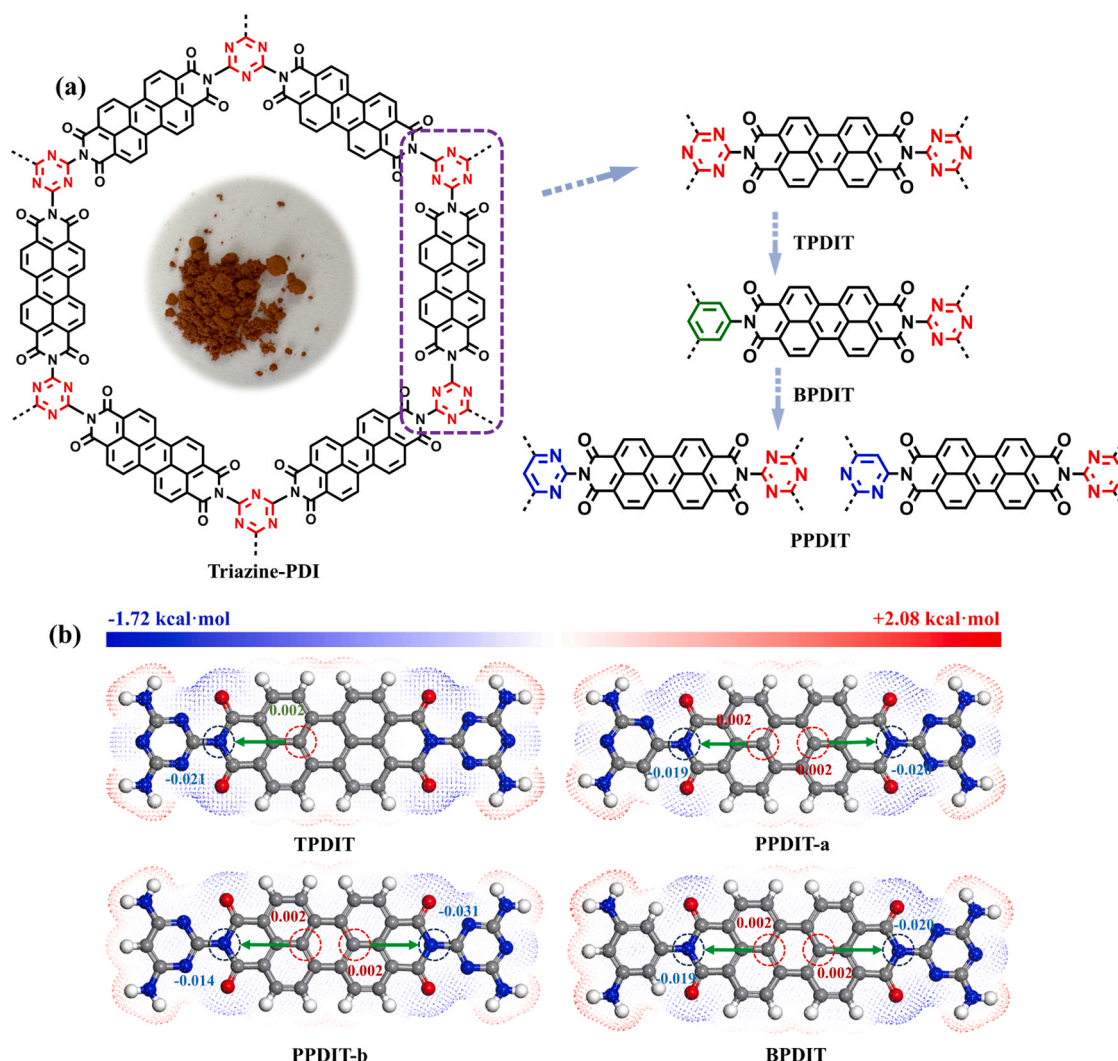


Fig. 1. (a) Schematic representation of the triazine structure in triazine-PDI substituted by benzene and pyrimidine structures, respectively and (b) electronic structure distribution and dipole moment labeling of TPDIT, PPDIT-a, PPDIT-b and BPDIT.

dipole moments within the PDI monomers can form a stronger spatial electric field to promote the rapid migration of photogenerated carriers; and (iii) covalently bonded PDI polymers have a high structural stability [19–22]. Although linking PDI monomers with covalent bonds to form PDI polymers is an effective strategy, the selection of the linking molecules therein and their influence on the charge transfer efficiency need to be further investigated and explored [23–26].

The construction of highly crystalline PDI polymers is a prerequisite for their carrier mobility, and the polarity of the joining molecules is crucial. PDI has small intramolecular dipoles, resulting in insufficient driving force for photogenerated charge generation and separation [27–30]. Therefore, the choice of the linking molecule must satisfy the need to possess a certain polarity without disrupting the overall crystallinity of the catalyst in order to induce a strong in-built electric field within the molecule [30,31]. In particular, it was found by comparison that triaminopyrimidine and triaminobenzene are small molecule structures similar to the melamine molecule. Therefore, in order to increase the degree of asymmetry of the system and to generate a stronger built-in electric field in the PDI molecule, the introduction of triaminopyrimidine and triaminobenzene into triazine-PDI can be considered [18]. As shown in Fig. 1a, the triazine structure in triazine-PDI (TPDIT) is replaced with benzene and pyrimidine structures to form BPDIT and PPDIT structures, respectively (two possible forms are listed in the PPDIT structure: PPDIT-a, PPDIT-b). Triaminopyrimidine and triaminobenzene

have triazine-like pyrimidine and benzene ring structure, which satisfy the requirement of having a certain polarity without destroying the overall crystallinity of the catalyst. In contrast, pyrimidine has a higher asymmetry compared to benzene and triazine, which makes it easier to induce a stronger built-in electric field in the PDI molecule.

In this study, PDI-based photoelectrodes with TPP and TBP structures formed by triazine-pyrimidine and triazine-benzene linked PDI were prepared. Both TPP and TBP showed better photoelectrocatalytic performance under the same light and bias conditions, and the current density of TPP reached 0.637 mA/cm² being 10.79 times higher than that of pure TP at 1.23 V vs. RHE. In addition, the free energies of oxygen evolution of the three structures were calculated by DFT to explain the catalytic mechanism of the photo-electrodes. This study provides a basis for the application of photoelectrocatalysts of PDI polymers in the field of new energy.

2. Experimental section

2.1. Synthesis

2.1.1. Synthesis of TP

Firstly, 6 g of imidazole was configured to which 0.2 mmol of 3, 4, 9, 10-Perylenetetracarboxylic dianhydride and 1 mmol of 1, 3, 5-triazine-2, 4, 6-triamine were added. The mixture was mixed well and heated,

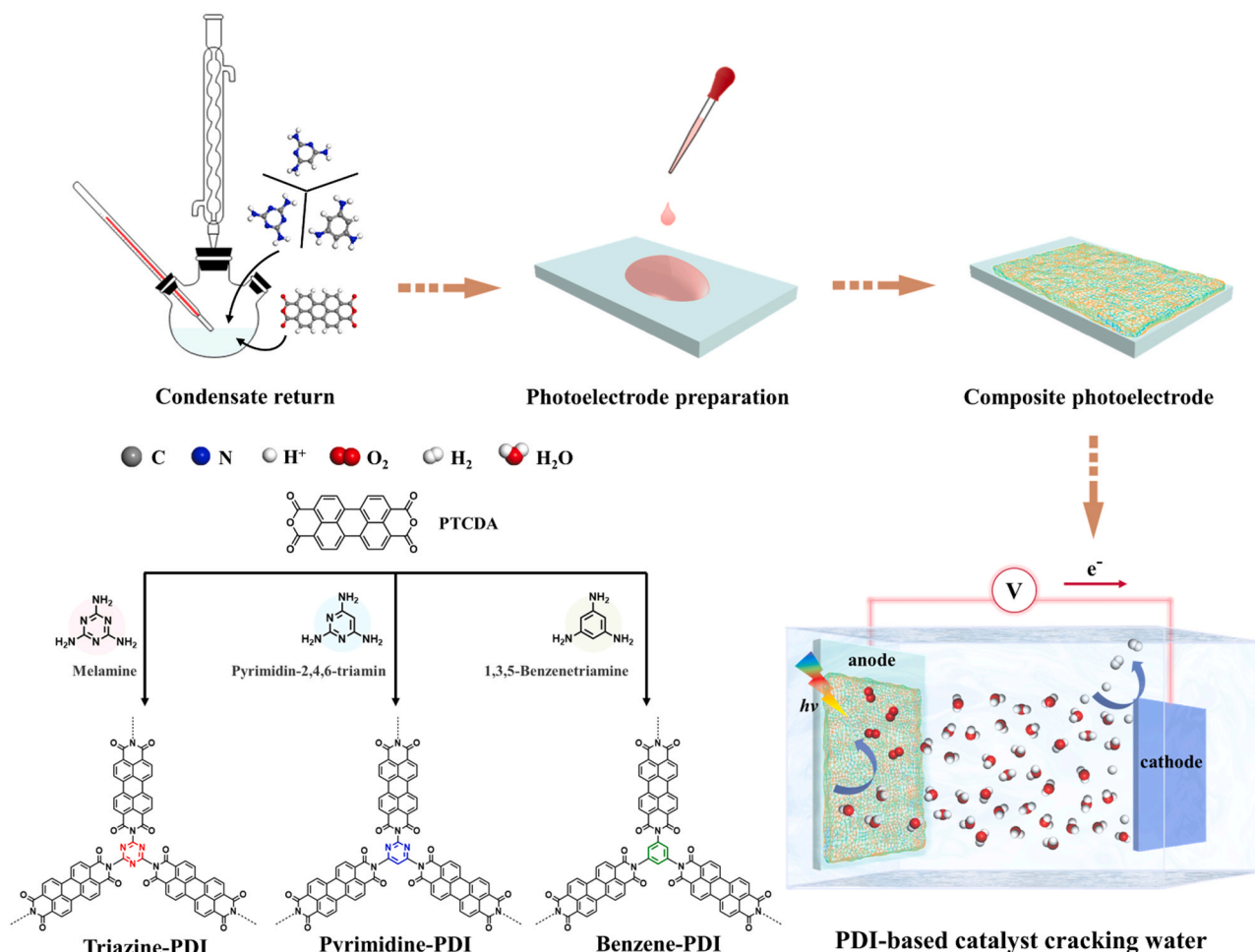


Fig. 2. Experimental flowchart for the preparation of TP, TPP and TBP and schematic structures of the three bridging molecules (triazine, pyrimidine and benzene structures).

the mixture gradually dissolved in reddish brown color and was refluxed after reaching 100°C for 6 h. Afterwards, the substrate was washed with anhydrous ethanol and centrifuged at 5000 r/s to obtain a fluorescent green supernatant and a reddish brown precipitate. The red-brown precipitate was separated and dried at 60°C for 10 h to obtain an orange powder (Fig. S1).

2.1.2. Synthesis of TPP

Firstly, 6 g of imidazole was configured to which 0.2 mmol of 3, 4, 9, 10-Perylenetetracarboxylic dianhydride, 0.9 mmol of 1, 3, 5-triazine-2, 4, 6-triamine and 0.1 mmol of 2, 4, 6-triaminopyrimidine were added. The mixture was mixed well and heated, the mixture gradually dissolved in reddish brown color and was refluxed after reaching 100°C for 6 h. After that, the substrate was washed with anhydrous ethanol and centrifuged at 5000 r/s to obtain fluorescent green supernatant and reddish brown precipitate. The red-brown precipitate was separated and dried at 60°C for 10 h to obtain a black-red powder (Fig. S2).

2.1.3. Synthesis of TBP

Firstly, 6 g of imidazole was configured to which 0.2 mmol of 3,4,9,10-Perylenetetracarboxylic dianhydride, 0.9 mmol of 1, 3, 5-triazine-2, 4, 6-triamine and 0.1 mmol of 1, 3, 5-triaminobenzene were added. The mixture was mixed well and heated, the mixture gradually dissolved in reddish brown color and was refluxed after reaching 100°C for 6 h. After that, the substrate was washed with anhydrous ethanol and centrifuged at 5000 r/s to obtain fluorescent green supernatant and reddish brown precipitate. The red-brown

precipitate was separated and dried at 60°C for 10 h to obtain a dark red powder (Fig. S3).

2.1.4. Preparation of PDI-based photoelectrodes

To 100 mg of a solution containing 5% Nafion and 1 mL of ethylene glycol was added 30 mg of the powder sample (TP/TPP/TBP) and stirred well. After that, the mixture was ultrasonically dispersed for 30 min, and drops were added to the clean FTO glass surface by gently shaking until the solution in spread. Finally, the photoelectrodes were obtained by drying at 60°C for 12 h.

2.2. Characterization

The samples underwent imaging with a scanning electron microscope (SEM) at 10 kV, while their microstructure was analyzed using both a JEM-2100 electron microscope and transmission electron microscope (TEM). Fourier transform infrared spectroscopy (FTIR) analyses were conducted at room temperature using a Nicolet 380 spectrophotometer within the spectral range of 600–4000 cm⁻¹, with a resolution of 4 cm⁻¹. Raman spectral results were obtained via a Renishaw Raman spectrometer. Ultraviolet-visible spectroscopy (UV-vis) was employed to determine the optical properties, utilizing a DU-8B instrument. Electrochemical characterization was performed in a 0.2 M sodium sulfate solution under simulated sunlight (AM 1.5 G, 100 mW·cm⁻², CHF-XM500) using a three-electrode electrochemical workstation. Photoluminescence (PL) spectra were analyzed with an RF-5301PC instrument to verify the carrier separation ability of the

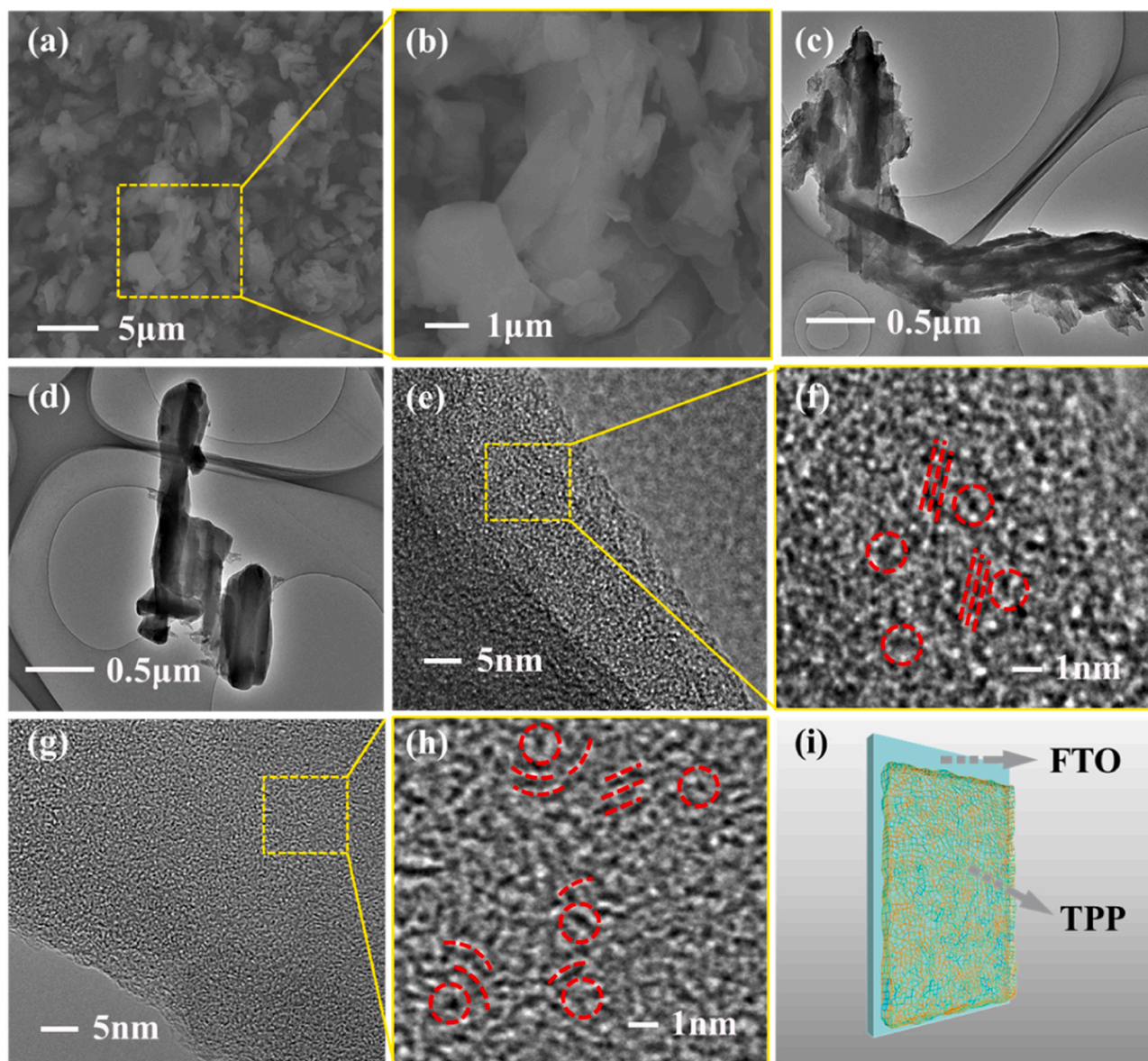


Fig. 3. (a), (b) SEM surface morphology and local magnification of TP, (c), (d) TEM image of TBP and TPP, (e), (f) HRTEM image and local magnification of TBP, (g), (h) HRTEM image and local magnification of TPP, and (i) Schematic diagram of network-like structure of TPP.

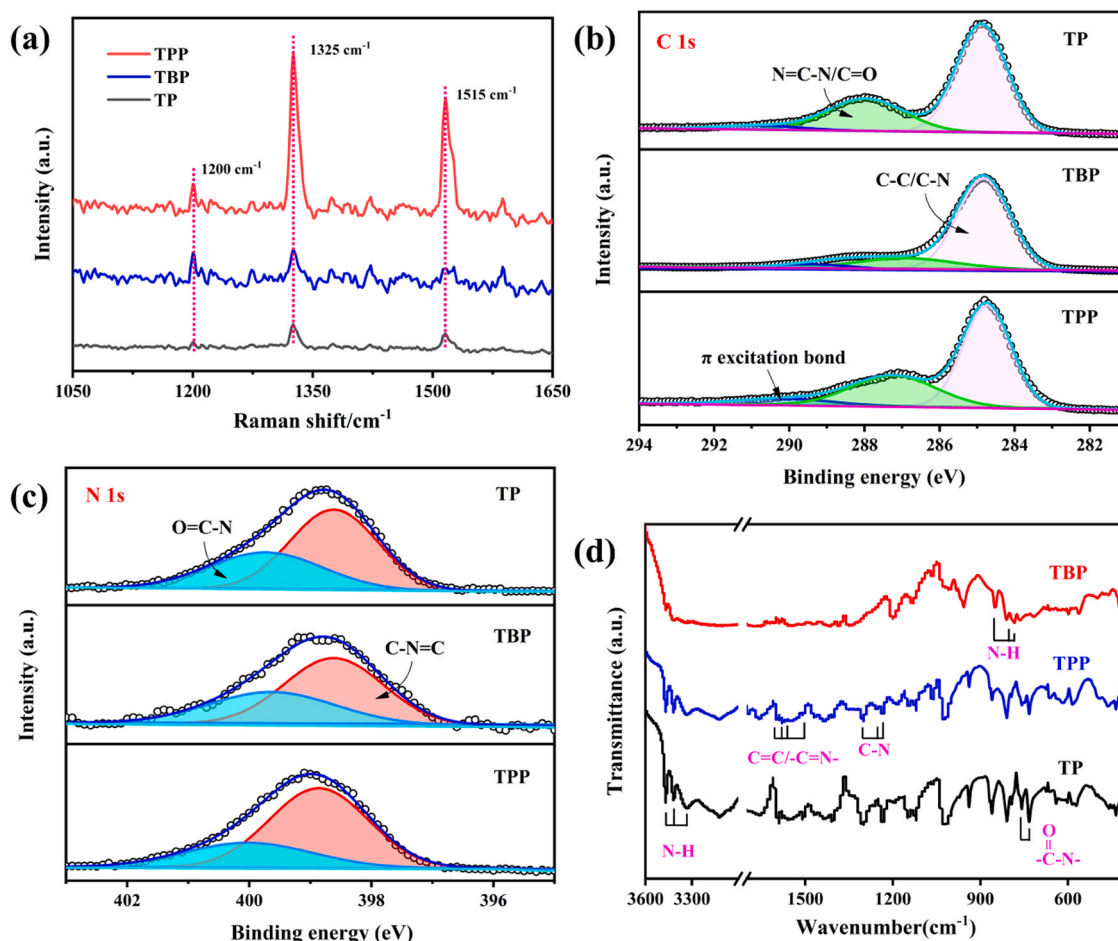


Fig. 4. (a) Raman spectra, (b) C 1 s XPS spectra, (c) N 1 s XPS spectra and (d) FTIR spectra of TP, TPP and TBP.

photocatalyst. All density functional theory (DFT) calculations were executed in Materials Studio 2019 software, employing the FORCITE module m-GGA (M06-L) for structure optimization and energy calculations on TP, TPP, and TBP structures. Further test details are provided in Supplementary Note.

3. Results and discussion

The potential distributions and electron counts of several structures were calculated using density-functional theory (DFT), and the dipole moments from the center C to the imine N of several structures were further calculated from the electron counts [32]. From the calculations (Fig. 1b), the dipole moment in the PPDIT-b structure near the triazine side of the structure (0.793 Debye (D)) is much larger than the dipole moment near the pyrimidine side (0.033 D) and the other structures. This result may be due to the fact that both pyrimidine N atoms are concentrated on the PDI side of the molecule, and the concentration of electrons breaks up the charge distribution, causing the negative charge center of the molecule to move to the right, resulting in a larger dipole moment. However, the large dipole moment is not observed in BPDIT, which may be attributed to the fact that the lower polarity of the benzene structure has a weaker effect on the charge than the triazine and pyrimidine, and does not have much effect on the overall space charge to the right. The presence of the benzene structure promotes the stability of the structure and the extension of the conjugated system, which also favors intramolecular charge conduction. At the same time, the three structures have high reactivity and are often used as electrophilic reagents, which also ensures the normal progress of low-temperature polymerization reactions. The sample preparation and

photoelectrochemical testing are schematically shown in Fig. 2.

The morphology and structure of the samples were characterized by scanning electron microscopy (SEM) and transmission electron microscopy (TEM). As shown in Fig. 3a, b the SEM morphology of TP, it can be observed that the samples are rod-like and granular. Similarly, TBP and TPP also have rod-like and granular morphology, but the morphology is more regular as observed from the TEM images (Figs. 3c, d, S4a-b). Further observation of the microstructure of the materials by HRTEM (Fig. 3e-h) reveals the presence of a ring structure with a diameter of about 0.6–0.7 nm in TBP and TPP. Meanwhile, streaks similar to the crystalline structure were distributed around this structure, respectively; in particular, the streak structure appeared in TPP was slightly curved in an arc shape. The linear stripes appearing in TBP are due to the π - π stacking of the benzene ring with the benzene/triazine ring. However, the shorter curved stripe structure in TPP is due to π - π stacking of pyrimidine ring with pyrimidine ring, triazine ring, and benzene ring (which are present on the PDI molecule), and lattice bending caused by large spatial site resistances resulting from the asymmetry of the pyrimidine ring structure [33,34]. In contrast, arcuate streaks are more abundant in the TPP structure than in the TBP. As a result, a TPP-like mesh structure was drawn (Fig. 3i), with planar surfaces connected by rings and vertical structures distributed in curved stacks.

To determine the stacking between the layers of the sample, in the Raman spectrum (Fig. 4a), the peak at 1515 cm^{-1} corresponds to the C-C/C=C bond, which is sensitive to π - π stacking interactions (noted as peak a). Meanwhile, the peak at 1325 cm^{-1} is associated with the in-plane bending of C-H, which is insensitive to π - π interactions (noted as peak b). Therefore, the strength of the π - π interaction of the sample can be indicated by the peak intensity ratio I ($I = I_a/I_b$) [35,36]. The π - π

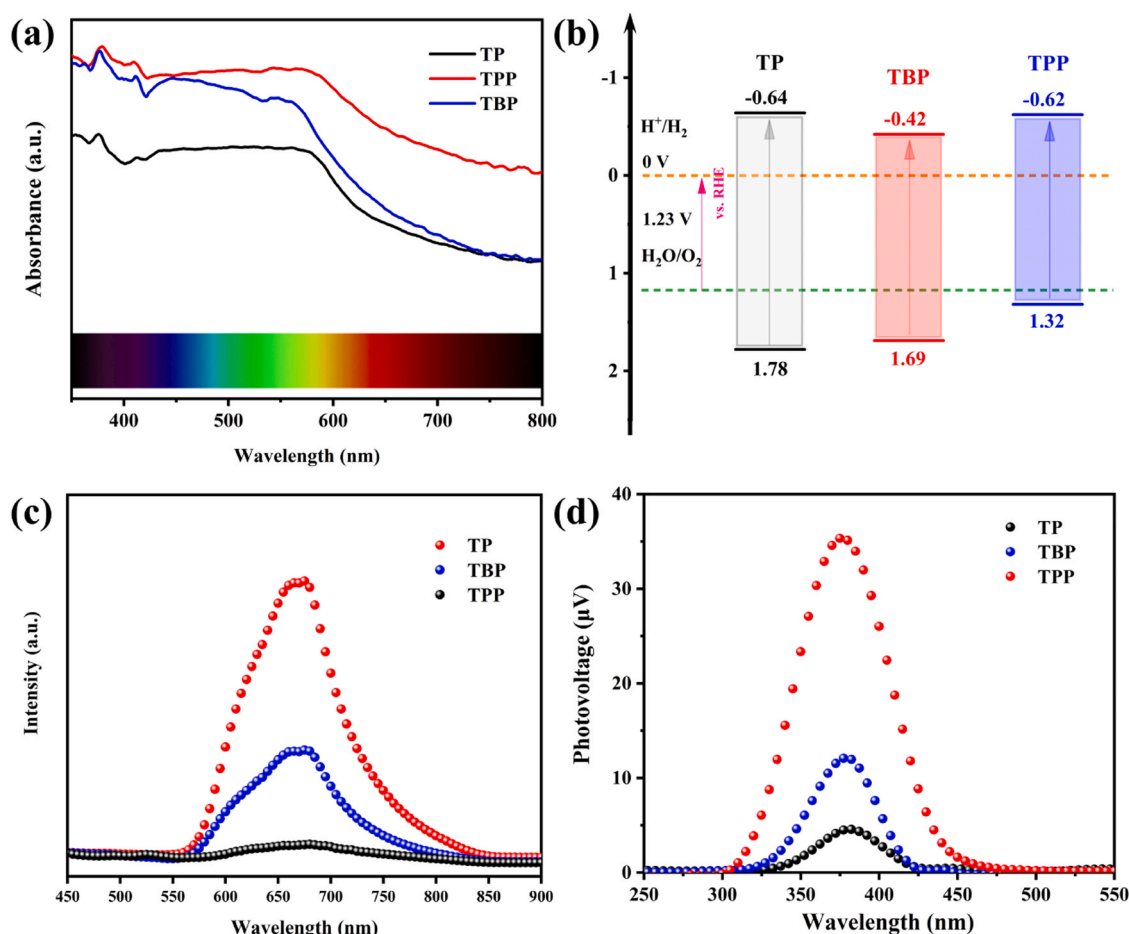


Fig. 5. (a) UV-vis spectrograms, (b) energy band structure maps, (c) comparison of PL spectra and (d) SPV spectrograms of TP, TPP and TBP.

interaction strengths were calculated to be 1.11, 1.08 and 1.05 for TPP, TBP and TP, respectively, i.e., $I_{TPP} > I_{TBP} > I_{TP}$. This result reflects that TPP has better π - π interactions, which are favorable for the stacking of lamellar structures and the transfer of charge between the layers.

The surface chemical states of TPP, TBP and TP were investigated using X-ray photoelectron spectroscopy (XPS) analysis. As shown in Fig. 4b, three peaks appeared in the XPS spectrum of C near 284.8 eV and 287.4 eV, which corresponded to the C-C/C-N and N=C-N/C=O bonds present in the sample, respectively. The intensity of the N=C-N peaks is weaker in TBP than in TP due to the lower number of triazine structures, but the intensity of the peaks corresponding to the pyrimidine structure in TBP is closer to that of the peaks corresponding to the pyrimidine structure in TP. It is noteworthy that the peak near 290.05 eV corresponds to the π -excited bond in PDI [34]. The electronic distribution of the carriers can be further determined by comparing the peak intensities of the three substances, TP, TBP and TPP, at this location. As shown in Table S1, it can be found that TPP possesses the highest π -excitation intensity at this location, and thus it can be judged that the stronger polar structure within TPP contributes to the change of the electronic structure of the PDI molecule. Further characterization of the content of functional groups corresponding to N elements in the samples can determine the types of linked small molecules in the samples. In the XPS spectrum of N (Fig. 4c), the peaks at 398.1 eV and 399.43 eV correspond to C=N=C and O=C-N bonds, respectively [35]. The differences in linked small molecules in the three samples can be further determined by comparing the O=C-N and C-N=C peak intensities (Table S2). The O=C-N peaks of the three samples varied with the addition of small molecules but were relatively close. However, the intensity of the C-N=C peak in the TBP sample is significantly weaker than

that in the TP and TPP samples, and it can be inferred that the addition of the benzene ring reduces the number of this functional group relative to TP and TPP. The localized XPS spectra of the samples are illustrated in Fig. S5, which also shows that the N peak intensity is lower on the TBP curve, while TP and TPP are close.

The Fourier transform infrared spectra (FT-IR) of TPP, TBP and TP are shown in Fig. 4d. The peaks near 1550 cm^{-1} are due to the C=C and C=N vibrations, the peaks between 1360 and 1200 cm^{-1} are attributed to the C-N telescoping vibrations, and the peaks between 783 and 851 cm^{-1} are attributed to N-H bending vibrations [36]. A more detailed peak analysis between 1000 and 1800 cm^{-1} is shown in Figs. S6–S8. The peak between 3330 and 3470 cm^{-1} is attributed to N-H stretching vibration and the peaks at 735 cm^{-1} and 760 cm^{-1} are due to C(=O)-N-bending vibration [37]. The intensity of each of the above peaks is significantly stronger for TP and TPP than for TBP, while the peak intensity of TPP is also slightly stronger than that of TP. The stretching and bending vibrations of N-H can explain the lower N content in the structure of TBP compared to TP and TPP. Meanwhile, the vibrations near 1550 cm^{-1} can indicate that there are more C=N bonds in TPS and TPP thus with higher peak intensities. In addition, the bending vibrations of C(=O)-N- at 735 cm^{-1} and 760 cm^{-1} can prove the presence of permethylenediimide backbone [38,39].

The ideal photoelectrode should have a broad visible spectral absorption response, suitable energy band structure, effective photoexcited carrier migration and separation efficiency. The optical properties of the samples were investigated by recording UV-visible spectra as shown in Fig. 5a. The optical properties of the samples were investigated by recording UV-vis spectra. The absorption spectra showed that the absorption bands of the three samples reached 550 – 800 nm , and the

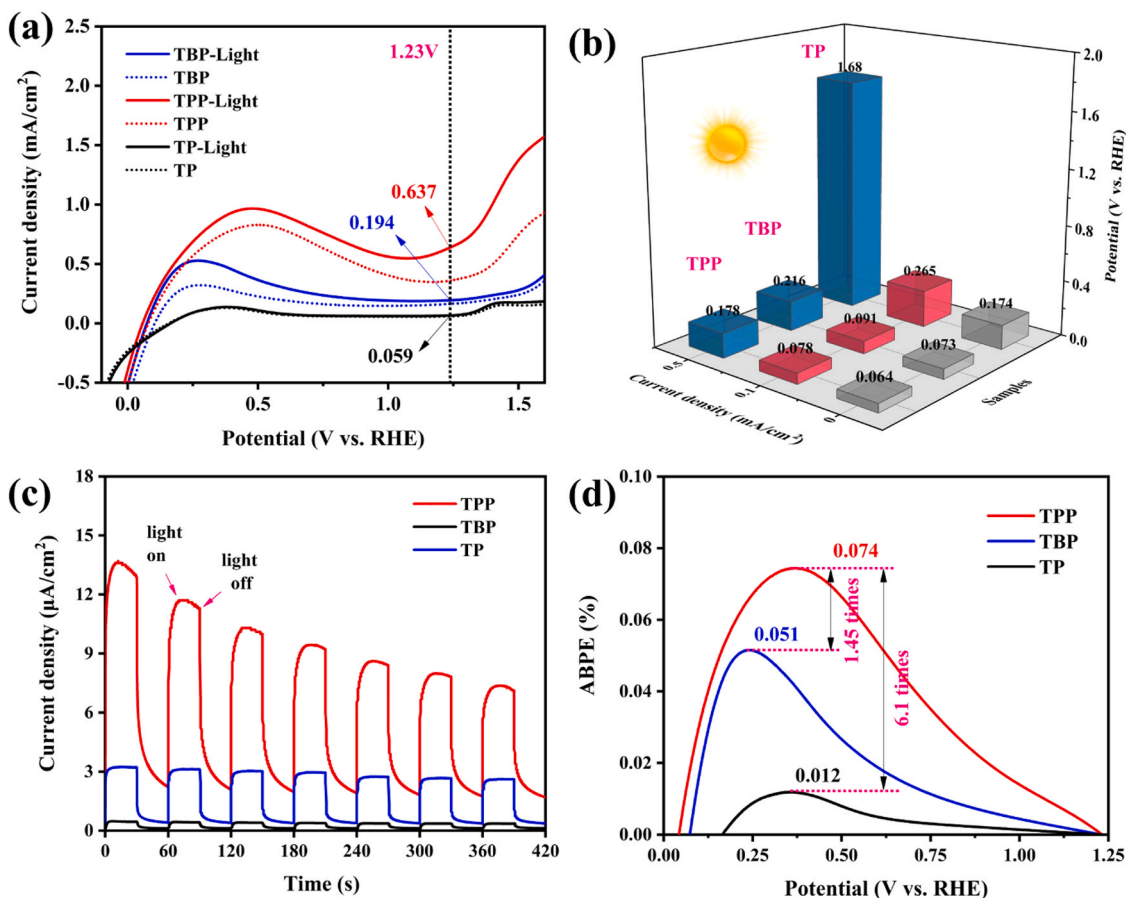


Fig. 6. (a) linear voltammetric curves, (b) overpotential comparisons, (c) 30 s light-dark alternating I-T test and (d) APBE curves of TP, TPP and TBP.

band gaps of the samples were obtained by calculating Tauc plots from the UV-vis spectra (Fig. S9) (see Supplementary Note for the calculation procedure). Among them, TPP has the relatively strongest light absorption capacity with a band gap of 1.94 eV, while TP also has a significant visible light absorption capacity with a band gap of 2.42 eV. The Mott Schottky (M-S) (Fig. S10) was used to determine the flat band potentials (flat band potentials) of TPP, TBP and TP with flat band potentials (E_f) of -0.52 eV, -0.32 eV and -0.54 eV (vs. RHE), respectively. Meanwhile, the samples all have positive slopes of M-S curves, all are n-type semiconductors, and the E_f is 0.1 eV larger than the conduction band (CB) [40]. Therefore, the conduction band positions of the three substances can be determined, and the valence band (VB) position and energy band structure can be further determined by combining with the band gap (Fig. 5b). Obviously, the energy band structures of the above electrodes all satisfy the thermodynamic conditions of water splitting well.

Photoluminescence spectroscopy (PL) is widely used to characterize the photogenerated charge separation efficiency of catalysts [41]. An emission peak at 670 nm was present for all three samples, and the highest emission intensity was present for TP, which can be attributed to the higher photogenerated electron-hole complexation rate of the catalyst (Fig. 5c). With the introduction of pyrimidine and benzene structures in the system, the luminescence intensity gradually decreases, indicating that the photogenerated electron-hole complexation is effectively suppressed in TPP and TBP. The surface photovoltage (SPV) technique was employed to further characterize the separation efficiency of the photogenerated charges of the samples [42]. As shown in Fig. 5d, the SPV signals of TP and TBP are weaker surface its higher carrier complexation rate. However, the improved SPV signal of TPP suggests that the presence of pyrimidine structures introduces a

polarized electric field to the system allowing space charges to accumulate on the surface.

Linear scanning voltammetry (LSV) curves of the prepared TPP, TBP and TP with a scan rate of 10 mV/s and no IR compensation for the electrodes. As shown in Fig. 6a, all of the above photocatalysts exhibited significant OER performance. Obviously, TPP has the lowest onset potential and the highest current density (1.23 V vs. RHE), reflecting the highest OER activity among the three substances. In addition, an oxidation peak could be observed for TPP at 0.5 V. To exclude the effect of the oxidation peak, the scanning direction of the LSV curves was adjusted (from positive to negative scanning, Fig. S11). It was found that the LSV curves were basically similar under positive and negative scans, with a slight decrease in current density at 1.23 V in the negative scan compared to the positive scan. However, TPP still has the lowest onset potential and the highest current density. Meanwhile, TPP also exhibited better electrocatalytic OER performance under light-free conditions, further demonstrating the superior light-assisted electrocatalytic OER performance of TPP. To further highlight the superiority of TPP electrode, Fig. 6b than also compares the overpotentials of the prepared catalysts at current densities of 100 $\mu\text{A}/\text{cm}^2$ and 500 $\mu\text{A}/\text{cm}^2$, respectively. It is noteworthy that TPP was able to reach the target current densities at 78 mV and 178 mV, which illustrates the ability of TPP to maintain a good catalytic efficiency at higher current densities. Further comparison of the activity of the samples was also made with the work of other researchers (Table S3). The OER onset voltages of some conventional organic/inorganic catalysts in recent years were compared, reflecting the high catalytic activity possessed by TP, TBP and TPP catalysts.

As shown in Fig. 6c, TP showed a photocurrent response of 0.322 $\mu\text{A}/\text{cm}^2$ under 30 s on/off illumination, indicating a high carrier

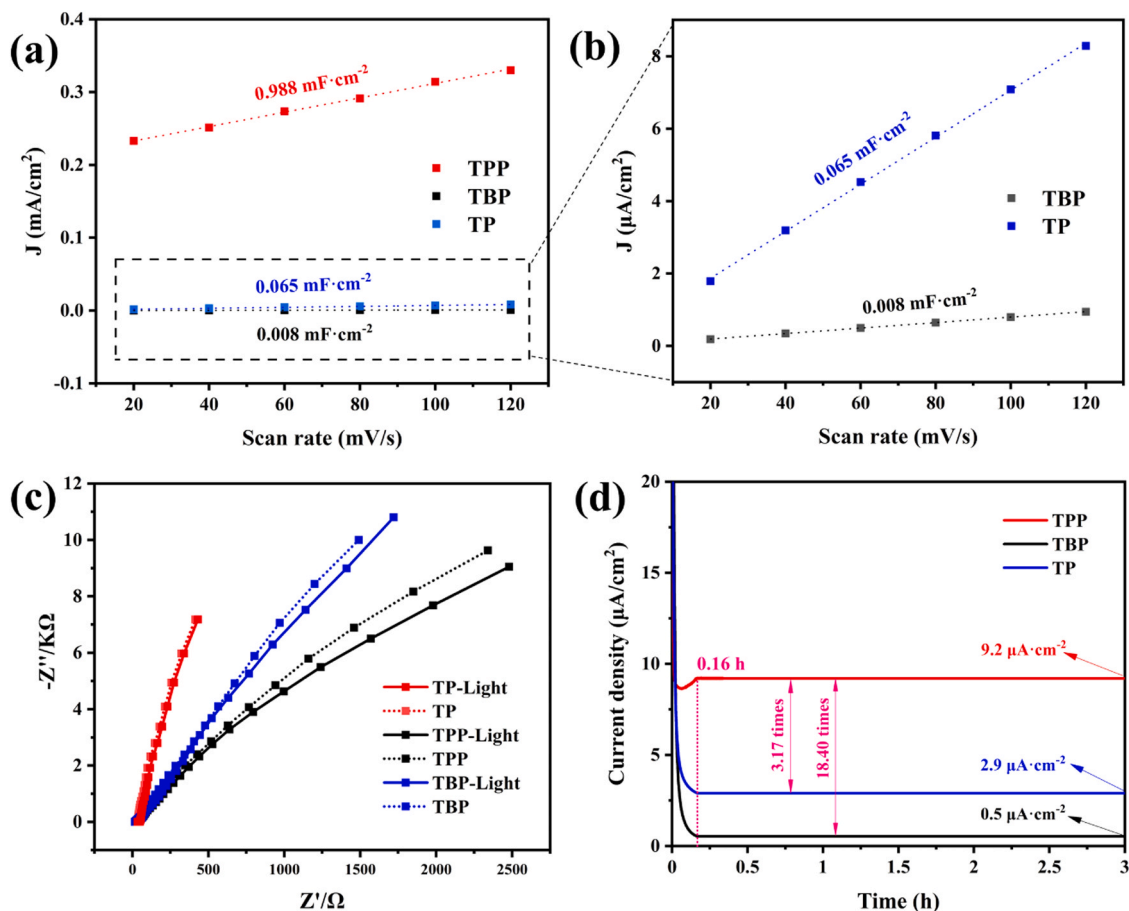


Fig. 7. (a), (b) Cdl curves, overpotential comparisons, (c) light-dark impedance mapping and (d) 3 h stability tests of TP, TPP and TBP.

complexation rate. However, TPP and TBP showed a greatly improved photocurrent response of $5.61 \mu\text{A}\cdot\text{cm}^{-2}$ and $2.29 \mu\text{A}\cdot\text{cm}^{-2}$, respectively, due to the introduction of polar groups. In addition, the applied bias photoelectric conversion efficiency (ABPE) was used to evaluate the water splitting ability of the electrodes (Fig. 6d). The TP photoelectrode had a light absorption efficiency of only 0.012%, whereas TPP and TBP could reach 0.074% and 0.051% are 6.10 and 1.45 times higher than that of TP, respectively.

Calculation of the electrochemically active surface area (ECSA) of the catalysts can be done by calculating the electrochemical double layer capacitance (Cdl) values from the CV curves at different sweep speeds (Figs. 7a, S12) [43,44]. It can be seen that the higher Cdl value of $0.988 \text{ mF}\cdot\text{cm}^{-2}$ for TPP is a significant improvement compared to TBP ($0.065 \text{ mF}\cdot\text{cm}^{-2}$) and TP ($0.008 \text{ mF}\cdot\text{cm}^{-2}$) with a large improvement. The above results can be attributed with the introduction of polar groups bringing more active sites to the catalyst. Electrochemical impedance spectroscopy (EIS) further confirmed the high OER catalytic activity of the TPP electrode, and the results are shown in Fig. 7b. In general, the smaller the radius of curvature of the Nyquist diagram, the faster the electron transfer kinetics of the reaction at the electrode surface and the lower the resistance to charge transfer (R_{ct}) (see Fig. S13 for the equivalent circuit at the electrode-electrolyte interface, and Table S4 for the fitted data). In contrast, TPP has the smallest radius of curvature, representing the fastest electron transfer rate and the smallest internal charge transfer resistance. Meanwhile, TPP had the smallest radius of curvature in both conditions with and without light, further confirming that the polar groups in TPP promoted carrier migration. In addition to high catalytic efficiency, the catalysts need to maintain stability for a long time. As

shown in Fig. 7c, the stability tests of the samples under light and applied 1.23 V (vs. RHE) for 3 h. It is noteworthy that all three samples can maintain a stable current density after 0.16 h. The catalysts of TPP are shown in Fig. 7d, which shows the stability of the catalysts. Among them, the current density of TPP is stable at $9.2 \text{ mA}/\text{cm}^2$, which is 3.17 and 18.40 times higher than that of TBP and TP, respectively.

Density Functional Theory (DFT) calculations of the electronic structure of materials to reveal the catalytic mechanism of catalysts is a commonly used research method [45,46]. The potential distributions and electron transfer numbers of the four structures were first calculated, as shown in Figs. S14 and S15, the four molecules have the lowest number of transferred electrons and the lowest positive charge density for the C atoms at the central positions (1^* , 2^*). Selecting these two positions as the sites for oxygen evolution allows estimation of the lowest oxygen evolution activity of the catalysts. Therefore, the Gibbs free energy (ΔG) of the oxygen evolution reaction was calculated for the four structures. From the calculations (Figs. 8a-d, S16, and S17 shows the schematic diagram of the oxygen evolution of PPDIT-b), the decisive speed step of the reactions of TPDIT, PPDIT-a-1*, PPDIT-b and BPDIT-2* is the formation of the intermediate state $^*\text{OOH}$ as O_2 , and the decisive speed step of the reactions of BPDIT-1* and PPDIT-a-2* is the formation of the intermediate state $^*\text{OH}$ as $^*\text{O}$. Among the four structures, three of the reaction free energies of the decisive step satisfy $\Delta G_1^* < \Delta G_2^*$, except for BPDIT where the opposite is true ($\Delta G_1^* > \Delta G_2^*$). This may be due to the lower polarity of the benzene ring structure, which makes oxygen evolution more difficult for the C atoms close to its side. Meanwhile, the activation energies of the decisive fast-step reactions of PPDIT-a are both higher with PPDIT-b probably due to the different

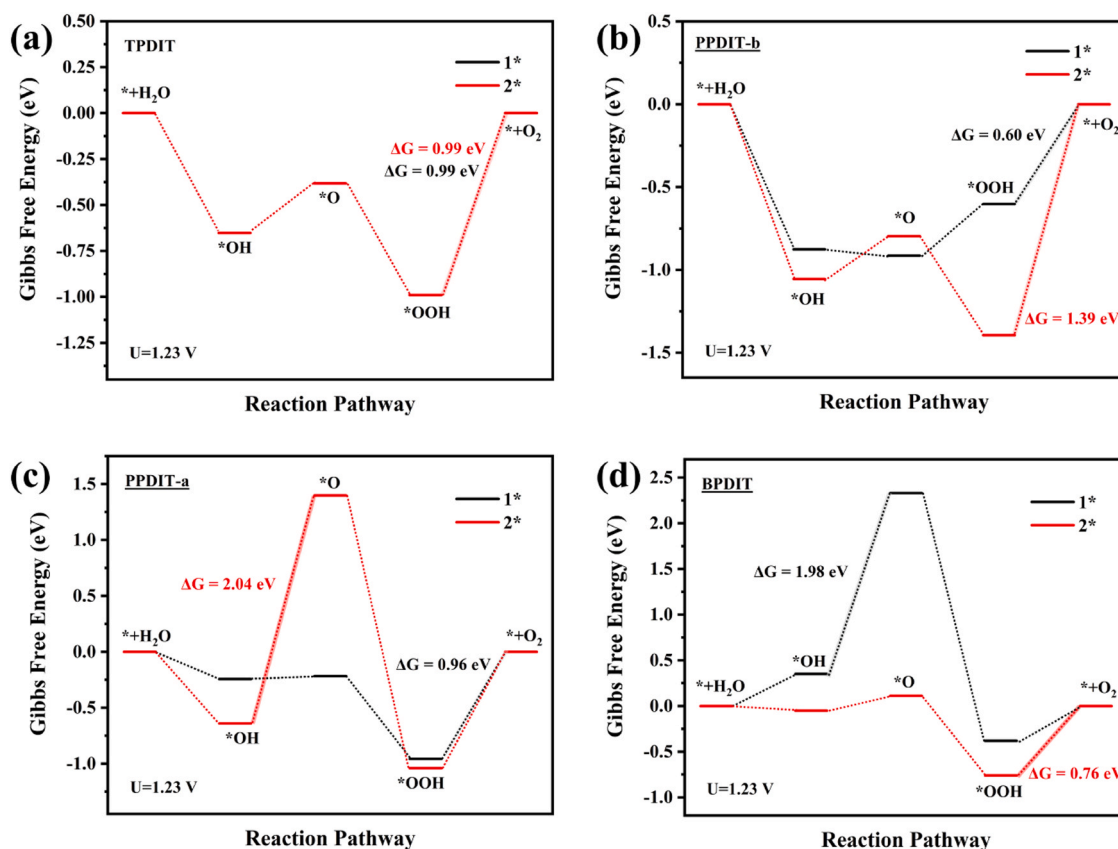


Fig. 8. Oxygen evolution free energy calculations for (a) TPDIT, (b) PPDIT-a, (c) PPDIT-b and (d) BPDIT at positions 1* and 2*.

attachment sites of the left linker molecules, and the two pyrimidine N atoms close to PPDIT-b have stronger polarity more favorable for the oxygen evolution at the 1*, 2* positions. The ΔG of PPDIT-b-1* is the smallest (0.60 eV), which also explains the highest OER activity of TPP structure. The above results can indicate that the molecular structure close to the pyridine N side has a stronger O_2 evolution activity, which is due to the strong electron-absorbing ability of pyridine N that makes the electrons to gather, while the vacancies are several in the PDI molecules with larger conjugated structures to improve the OER activity.

Based on this, the reaction mechanism of TPP photoelectrocatalytic splitting of water was proposed (Fig. 9). When there is light irradiation to the surface of TPP photoelectrode, photoelectrons and holes are generated, and the electrons reach to the counter electrode under external bias to participate in the H_2 evolution process through the external circuit. At the same time, holes are transported to the electrode surface to participate in the O_2 evolution process through the conjugated structure of the system (interlayer π - π stacking, conjugated structure of PDI molecules). In this case, the bridging molecules provide the polarity of the electrode as a whole, constructing a spatial electric field will help the separation and transport of electrons and holes.

4. Conclusion

In summary, PDI-based photoelectrodes with TPP and TBP structures formed by triazines, pyrimidines and benzene linked to PDI were prepared using a simple organic synthesis, which improved the overall carrier transport efficiency and reactivity of the catalysts. DFT calculations and experimental characterization were able to demonstrate that in the presence of the bridging molecules triazine, pyrimidine and benzene in the system, their interactions form a complex and ordered

spatial electric field. The presence of this electric field promotes the migration of carriers in the system, contributes to the lowering of the energy barrier for the O_2 evolution reaction and increases the reactivity of the surface. Furthermore, it was observed that TPP and TBP exhibited an extended sunlight response range, increased reactivity and improved carrier kinetics in this system. In particular, the current density of TPP reached 0.637 mA/cm^2 at 1.23 V vs. RHE, which is a 10.79-fold increase compared to pure S. This study provides a new idea and development direction for the application of PDI polymer photocatalysts in the new energy field.

CRediT authorship contribution statement

Weixing Nie: Writing – original draft, Formal analysis, Data curation. **Mengnan Ruan:** Funding acquisition, Conceptualization. **Bo Li:** Methodology. **Yuxin Sun:** Investigation. **Ke Ruan:** Methodology. **Xiaowei Liu:** Writing – review & editing. **Zhifeng Liu:** Writing – review & editing, Conceptualization.

Declaration of Competing Interest

The authors declare that they have no known competing financial interests or personal relationships that could have appeared to influence the work reported in this paper.

Data availability

Data will be made available on request.

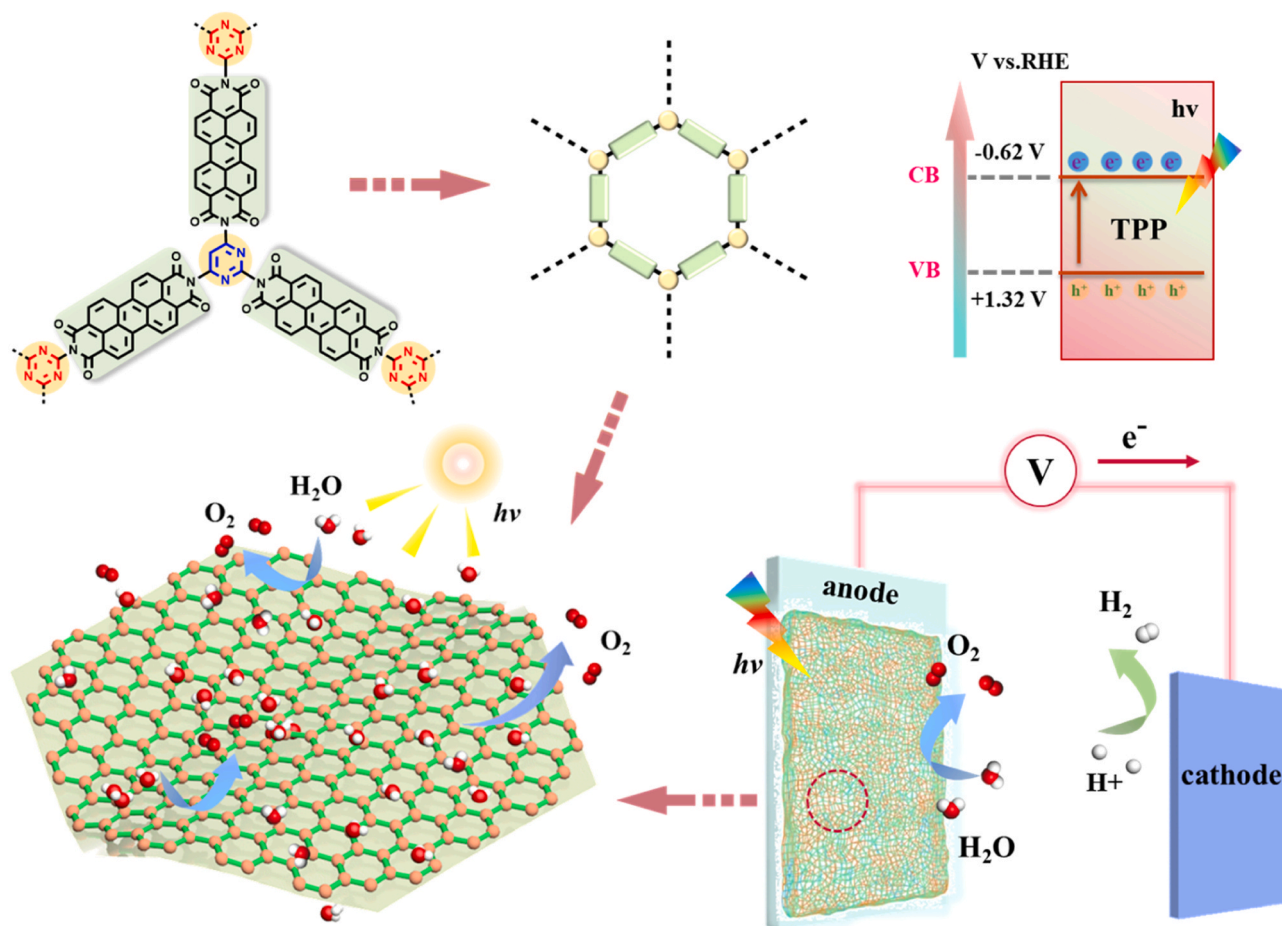


Fig. 9. Mechanistic diagram of photoelectrocatalytic splitting of water by TPP.

Acknowledgments

The authors gratefully acknowledge financial support from the Tianjin Science and Technology Planning Project (21YDTPJC00730) and National Natural Science Foundation of China (No. 52373301).

Appendix A. Supporting information

Supplementary data associated with this article can be found in the online version at [doi:10.1016/j.apcatb.2024.124242](https://doi.org/10.1016/j.apcatb.2024.124242).

References

- [1] R. Changotra, A.K. Ray, Q. He, Establishing a water-to-energy platform via dual-functional photocatalytic and photoelectrocatalytic systems: a comparative and perspective review, *Adv. Colloid Interface Sci.* 309 (2022) 102793.
- [2] K. Poonia, P. Singh, A. Singh, et al., Photoelectrocatalytic systems for simultaneous energy recovery and wastewater treatment: a review, *Environ. Chem. Lett.* 21 (2023) 265–283.
- [3] Y. Miao, Z. Li, Y. Song, et al., Surface active oxygen engineering of photoanodes to boost photoelectrochemical water and alcohol oxidation coupled with hydrogen production, *Appl. Catal. B Environ.* 323 (2023) 122147.
- [4] H. Lu, X. Li, S.A. Monny, et al., Photoelectrocatalytic hydrogen peroxide production based on transition-metal-oxide semiconductors, *Chin. J. Catal.* 43 (2022) 1204–1215.
- [5] T. Tong, M. Zhang, W. Chen, et al., Recent advances in carbon-based material/semiconductor composite photoelectrocatalysts: synthesis, improvement strategy, and organic pollutant removal, *Coord. Chem. Rev.* 500 (2024) 215498.
- [6] H. Zhu, D. Liu, D. Zou, et al., The photo-, electro- and photoelectrocatalytic properties and application prospects of porous coordinate polymers, *J. Mater. Chem. A* 6 (2018) 6130–6154.
- [7] X. Bai, C. Wang, X. Wang, et al., Strong electron affinity PDI supramolecules form anion radicals for the degradation of organic pollutants via direct electrophilic attack, *Catal. Sci. Technol.* 11 (2021) 1899–1913.
- [8] H. Li, C. Wang, X. Bai, et al., In-plane polarization induced by the hydrogen bonding and π - π stacking of functionalized PDI supramolecules for the efficient photocatalytic degradation of organic pollutants, *Mater. Chem. Front.* 4 (2020) 2673–2687.
- [9] J. Wang, W. Shi, D. Liu, et al., Supramolecular organic nanofibers with highly efficient and stable visible light photooxidation performance, *Appl. Catal. B Environ.* 202 (2017) 289–297.
- [10] X. Bai, B. Sun, C. Wang, et al., Microwave-initiated recombination of hydrogen bonds of a perylene diimide supramolecule for PPCP photodegradation, *Catal. Sci. Technol.* 11 (2021) 3787–3798.
- [11] A.S. Jalilov, L.G. Nilewski, V. Berka, et al., Perylene diimide as a precise graphene-like superoxide dismutase mimetic, *ACS Nano* 11 (2017) 2024–2032.
- [12] X. Liu, Z. Huang, Y. Huang, et al., Tunable supramolecular helical aggregate and optoelectrical properties of perylene diimides by stereoisomerism of sugar, *J. Phys. Chem. C* 121 (2017) 7558–7563.
- [13] J. Li, L. Cai, J. Shang, et al., Giant enhancement of internal electric field boosting bulk charge separation for photocatalysis, *Adv. Mater.* 28 (2016) 4059–4064.
- [14] J. Schneider, M. Matsuoka, M. Takeuchi, et al., Understanding TiO₂ photocatalysis: mechanisms and materials, *Chem. Rev.* 114 (2014) 9919–9986.
- [15] Y. Li, X.L. Zhang, D. Liu, Recent developments of perylene diimide (PDI) supramolecular photocatalysts: a review, *J. Photochem. Photobiol. C Photochem. Rev.* 48 (2021) 100436.
- [16] X. Chen, J. Wang, Y. Chai, et al., Efficient photocatalytic overall water splitting induced by the giant internal electric field of $\text{ag-C}_3\text{N}_4/\text{rGO}/\text{PDIP}$ Z-scheme heterojunction, *Adv. Mater.* 33 (2021) 2007479.
- [17] Z. Zhang, X. Chen, H. Zhang, et al., A highly crystalline perylene imide polymer with the robust built-in electric field for efficient photocatalytic water oxidation, *Adv. Mater.* 32 (2020) 1907746.
- [18] H. Zhang, X. Chen, Z. Zhang, et al., Highly-crystalline triazine-PDI polymer with an enhanced built-in electric field for full-spectrum photocatalytic phenol mineralization, *Appl. Catal. B Environ.* 287 (2021) 119957.
- [19] C. Huang, S. Barlow, S.R. Marder, Perylene-3, 4, 9, 10-tetracarboxylic acid diimides: synthesis, physical properties, and use in organic electronics, *J. Org. Chem.* 76 (2011) 2386–2407.
- [20] K.V. Rao, R. Haldar, T.K. Maji, et al., Porous polyimides from polycyclic aromatic linkers: selective CO₂ capture and hydrogen storage, *Polymer* 55 (2014) 1452–1458.

- [21] P. Sharma, D. Damien, K. Nagarajan, et al., Perylene-polyimide-based organic electrode materials for rechargeable lithium batteries, *J. Phys. Chem. Lett.* 4 (2013) 3192–3197.
- [22] Y. Liao, J. Weber, C.F.J. Faul, Fluorescent microporous polyimides based on perylene and triazine for highly CO₂-selective carbon materials, *Macromolecules* 48 (2015) 2064–2073.
- [23] C. Yang, B.C. Ma, L. Zhang, et al., Molecular engineering of conjugated polybenzothiadiazoles for enhanced hydrogen production by photosynthesis, *Angew. Chem. Int. Ed.* 55 (2016) 9202–9206.
- [24] A. Liu, L. Gedda, M. Axelsson, et al., Panchromatic ternary polymer dots involving sub-picosecond energy and charge transfer for efficient and stable photocatalytic hydrogen evolution, *J. Am. Chem. Soc.* 143 (2021) 2875–2885.
- [25] B. Zhang, F. Wang, H. Zhou, et al., Polymer dots compartmentalized in liposomes as a photocatalyst for in situ hydrogen therapy, *Angew. Chem. Int. Ed.* 58 (2019) 2744–2748.
- [26] Y. Wang, A. Vogel, M. Sachs, et al., Current understanding and challenges of solar-driven hydrogen generation using polymeric photocatalysts, *Nat. Energy* 4 (2019) 746–760.
- [27] X. Jiang, C. Wang, G. Li, et al., Enhanced interfacial property and thermal conductivity of pitch-based carbon fiber/epoxy composites via three-layer assembly of PDI/GN/PDI interphase, *Compos. Part B Eng.* 273 (2024) 111238.
- [28] W. Chu, S. Tan, Q. Zheng, et al., Ultrafast charge transfer coupled to quantum proton motion at molecule/metal oxide interface, *Sci. Adv.* 8 (2022) eabo2675.
- [29] G. Zhang, Z.A. Lan, X. Wang, Conjugated polymers: catalysts for photocatalytic hydrogen evolution, *Angew. Chem. Int. Ed.* 55 (2016) 15712–15727.
- [30] L. Yang, Y. Xiong, L. Li, et al., Manipulation of charge transfer in FeP@Fe₂O₃ core-shell photoanode by directed built-in electric field, *ACS Appl. Energy Mater.* 1 (2018) 4591–4598.
- [31] J. Xu, W. Li, W. Liu, et al., Efficient photocatalytic hydrogen and oxygen evolution by side-group engineered benzodiazole oligomers with strong built-in electric fields and short-range crystallinity, *Angew. Chem. Int. Ed.* 61 (2022) e202212243.
- [32] A.N.A. Anasthasiya, P.K. Rai, B.G. Jeyaprakash, Understanding ammonia adsorption and charge transfer process on ZnO using experimental and DFT approach, *Mater. Chem. Phys.* 214 (2018) 540–547.
- [33] C. Wang, T. Huddle, E.H. Lester, et al., Quantifying curvature in high-resolution transmission electron microscopy lattice fringe micrographs of coals, *Energy Fuels* 30 (2016) 2694–2704.
- [34] L. González-Ronda, D.C. Martin, Lattice bending in electrooptically active poly (nonylbithiazole) and poly (nonylbisoxazole), *Macromolecules* 37 (2004) 2872–2879.
- [35] R. Chen, H. Lou, Y. Pang, et al., Enhancing pollutant mineralization through organic-inorganic defect-transit dual S-scheme with a robust internal electric field, *Small* 20 (2024) 2306354.
- [36] H. Seong, W. Nam, J.H. Moon, et al., Lithium storage mechanism: a review of perylene diimide N-substituted with a 1, 2, 4-triazol-3-yl ring for organic cathode materials, *ACS Appl. Mater. Interfaces* 15 (2023) 58451–58461.
- [37] T. Steiner, The hydrogen bond in the solid state, *Angew. Chem. Int. Ed.* 41 (2002) 48–76.
- [38] B. Fuerte-Díez, E. Rangel-Rangel, F. Sánchez, et al., Metal-free redox-active diphenylpyrenediimides: a comparison between the photocatalytic performance of molecular and polymeric catalysts, *J. Catal.* 428 (2023) 115156.
- [39] X. Wang, J. Meng, X. Yang, et al., Fabrication of a perylene tetracarboxylic diimide-graphitic carbon nitride heterojunction photocatalyst for efficient degradation of aqueous organic pollutants, *ACS Appl. Mater. Interfaces* 11 (2018) 588–602.
- [40] X. Gao, J. Chen, H. Che, et al., Rationally constructing of a novel composite photocatalyst with multi charge transfer channels for highly efficient sulfamethoxazole elimination: mechanism, degradation pathway and DFT calculation, *Chem. Eng. J.* 426 (2021) 131585.
- [41] L. Wang, Y. Hu, F. Qi, et al., Anchoring black phosphorus nanoparticles onto ZnS porous nanosheets: efficient photocatalyst design and charge carrier dynamics, *ACS Appl. Mater. Interfaces* 12 (2020) 8157–8167.
- [42] W. Shi, F. Guo, M. Li, et al., N-doped carbon dots/CdS hybrid photocatalyst that responds to visible/near-infrared light irradiation for enhanced photocatalytic hydrogen production, *Sep. Purif. Technol.* 212 (2019) 142–149.
- [43] C.C.L. McCrory, S. Jung, J.C. Peters, et al., Benchmarking heterogeneous electrocatalysts for the oxygen evolution reaction, *J. Am. Chem. Soc.* 135 (2013) 16977–16987.
- [44] T. Liu, P. Li, N. Yao, et al., CoP-doped MOF-based electrocatalyst for pH-universal hydrogen evolution reaction, *Angew. Chem.* 131 (2019) 4727–4732.
- [45] A. Kulkarni, S. Siahrostami, A. Patel, et al., Understanding catalytic activity trends in the oxygen reduction reaction, *Chem. Rev.* 118 (2018) 2302–2312.
- [46] J.K. Nørskov, J. Rossmeisl, A. Logadottir, et al., Origin of the overpotential for oxygen reduction at a fuel-cell cathode, *J. Phys. Chem. B* 108 (2004) 17886–17892.